

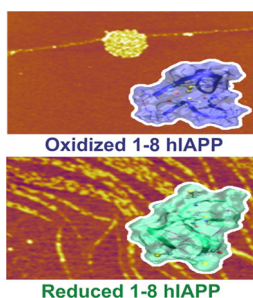
# Human Islet Amyloid Polypeptide N-Terminus Fragment Self-Assembly: Effect of Conserved Disulfide Bond on Aggregation Propensity

Alexandre I. Ilitchev,<sup>1</sup> Maxwell J. Giammona,<sup>1</sup> Thanh D. Do,<sup>1</sup> Amy G. Wong,<sup>2</sup>  
Steven K. Buratto,<sup>1</sup> Joan-Emma Shea,<sup>1</sup> Daniel P. Raleigh,<sup>2,3</sup> Michael T. Bowers<sup>1</sup>

<sup>1</sup>Department of Chemistry and Biochemistry, University of California, Santa Barbara, CA 93106, USA

<sup>2</sup>Department of Chemistry, Stony Brook University, Stony Brook, NY 11794-3400, USA

<sup>3</sup>Research Department of Structural and Molecular Biology, University College London, Gower Street, London, WC1E 6BT, UK



**Abstract.** Amyloid formation by human islet amyloid polypeptide (hIAPP) has long been implicated in the pathogeny of type 2 diabetes mellitus (T2DM) and failure of islet transplants, but the mechanism of IAPP self-assembly is still unclear. Numerous fragments of hIAPP are capable of self-association into oligomeric aggregates, both amyloid and non-amyloid in structure. The N-terminal region of IAPP contains a conserved disulfide bond between cysteines at position 2 and 7, which is important to hIAPP's *in vivo* function and may play a role in *in vitro* aggregation. The importance of the disulfide bond in this region was probed using a combination of ion mobility-based mass spectrometry experiments, molecular dynamics simulations, and high-resolution atomic force microscopy imaging on the wildtype 1-8 hIAPP fragment, a reduced fragment with no disulfide bond, and a fragment with both cysteines at positions 2 and 7 mutated to serine. The results indicate the wildtype fragment aggregates by a different pathway than either comparison peptide and that the intact disulfide bond may be protective against aggregation due to a reduction of inter-peptide hydrogen bonding.

**Keywords:** Amyloid, IAPP, Islet amyloid polypeptide, Diabetes, T2DM, Type 2 diabetes mellitus, human Islet Amyloid Polypeptide, hIAPP, Ion mobility, Electrospray ionization, Peptide, Atomic force microscopy, Replica exchange molecular dynamics

Received: 25 November 2015/Revised: 11 January 2016/Accepted: 12 January 2016/Published Online: 19 February 2016

## Introduction

Increasing evidence correlates the process of amyloid formation by human islet amyloid polypeptide (hIAPP) with pathogenic  $\beta$ -cell apoptosis in diabetes mellitus type II (T2DM) [1–8]. hIAPP is a 37-residue peptide co-secreted with insulin from pancreatic  $\beta$ -cells, which normally plays an adaptive role in glucose metabolism. In T2DM this peptide is overexpressed and misfolds from its natively disordered state [8–11], forming pervasive amyloid plaques in the pancreas. Amyloid formation

by hIAPP also contributes to the failure of islet transplants [12, 13]. As with other amyloid diseases, hIAPP plaques are composed of macroscopic, structured fibrils containing stacked parallel protein  $\beta$ -sheets [1, 14]. Recent findings suggest that it is not the plaques but early soluble oligomers that are the most pathogenic agent [2, 3, 15, 16]. It is therefore critical to understand early oligomer assembly and structure, a process hampered by the transient nature of the soluble oligomers. Ion mobility spectrometry-mass spectrometry (IMS-MS) has proven to be a powerful tool for investigating the distribution of these low-order amyloid oligomers [17–21]. Previous IMS-MS studies have revealed key differences between the oligomers formed by hIAPP and the oligomers formed by nontoxic rat IAPP [22, 23]. IMS-MS has also been used to study the inhibition of hIAPP amyloid formation *in vitro* by insulin and small molecules [20, 21, 24].

**Electronic supplementary material** The online version of this article (doi:10.1007/s13361-016-1347-7) contains supplementary material, which is available to authorized users.

Correspondence to: Michael T. Bowers; e-mail: bowers@chem.ucsb.edu

The aggregation dynamics of hIAPP peptide segments have been studied for their potential as aggregation nucleation sites while modified fragments serve as promising inhibitors of hIAPP aggregation [25–30]. Much attention has focused on hIAPP<sub>20-29</sub> (consisting of the 20–29 residue region, SNNFGAILSS) and hIAPP<sub>22-29</sub> as early work linked the primary sequence in this region to hIAPP amyloidogenicity. Subsequent work showed the situation is more complex but the 22–29 region is still considered to be a key contributor to hIAPP aggregation [31–33]. Several other IAPP segments have been found capable of self-association, including the N-terminal region [27, 34, 35]. This region, which contains an intramolecular disulfide bond between cysteine residues 2 and 7, is thought to be important to hIAPP's *in vivo* activity [36–38]. Additionally, while hIAPP has been found to endogenously decrease insulin secretion from  $\beta$ -cells, the introduction of hIAPP<sub>8-37</sub> had an antagonistic effect on hIAPP-mediated insulin inhibition [39]. There are conflicting reports on the role of the N-terminus in hIAPP aggregation; early studies showed that amyloid formation by an 8-37 fragment of hIAPP occurs more rapidly in buffer but more slowly in the presence of 1.5% hexafluoroisopropanol (HFIP) [40, 41]. In either case, the effect was modest but scanning transmission electron microscopy (STEM) appears to indicate that truncation changes the morphology of the fibrils [40]. A mutant form of hIAPP, with alanine substitutions at both cysteine residues, positions 2 and 7, showed a modest increase in the nucleation lag-phase compared with wildtype hIAPP [42]. A study by Cope et al. has shown that the hIAPP<sub>1-8</sub> peptide fragment is capable of non-amyloid aggregation into large macroscopic structures and that cleavage of the disulfide bond apparently inhibits this aggregation process [43]. Given both the physiological and biophysical significance of the disulfide bond in hIAPP, understanding the role of the N-terminal region is important to the overall picture of IAPP aggregation and pathology.

In this paper, we investigate the role of the N-terminus fragment in aggregation using a combination of ion-mobility mass spectrometry (IMS-MS), atomic force microscopy (AFM), and replica-exchange molecular dynamics (REMD) (Figure 1). IMS-MS allows for the separation of conformational isomers based on their cross section and, when coupled with a soft ionization source, clear characterization of isomeric and oligomeric species is possible [44, 45]. While the combination of ion mobility and molecular simulations allows for the determination of early small oligomer structures, AFM adds the

ability to observe bulk characteristics of the peptide in solution as well as larger oligomeric aggregates, which correlate with longer aggregation times [46–49]. By combining these methods, significant insight into the structural details of peptide oligomerization in solution can be obtained, particularly over a broad range of oligomer sizes.

## Materials and Methods

### Peptide Synthesis and Preparation

All peptides were synthesized using Fmoc-based microwave-assisted methods and purified by reverse-phase HPLC as previously described [50, 51]. All peptides contain an amidated C-terminus. Samples were dissolved in 100% hexafluoroisopropanol (HFIP) (Sigma-Aldrich, St. Louis, MO, USA) to a final stock concentration of 1mM. Aliquots of the stock were lyophilized and redissolved in 1:1 methanol:water for final peptide concentrations of 50–100 $\mu$ M. In order to reduce the disulfide bond between cysteine residues 2 and 7, *tris*(2-carboxyethyl)phosphine (TCEP) (Alfa Aesar, Ward Hill, MA, USA) was added at a 10:1 excess to peptide solutions and briefly incubated before measurements were taken. Reduction of the disulfide bond was verified via quadrupole time-of-flight mass spectrometry (Supplementary Figure S4). All solvents had their pH adjusted to physiological pH (7.4) using concentrated ammonium hydroxide and acetic acid unless otherwise noted.

### Ion Mobility Experiments

An in-depth description of the IMS-MS instrumentation has been given previously [52]. In summary, samples were loaded into gold-coated borosilicate glass capillaries that had been pulled to a fine point using an in-house capillary puller (Sutter Instrument Co., Novato, CA, USA). Using a nanoelectrospray ionization source (nano-ESI), ions are pulled from the capillary under the influence of a voltage differential and channeled through a small ( $\sim$ 70 $\mu$ m) orifice into an ion funnel. The funnel then collects and focuses the ions; these can either be continuously funneled (for mass spectra) or pulsed (for ion mobility) into a 4.5-cm drift cell filled with  $\sim$ 3.5Torr of helium gas. Under the influence of a weak electric field, ions are drifted through the cell, mass analyzed by a quadrupole, and detected

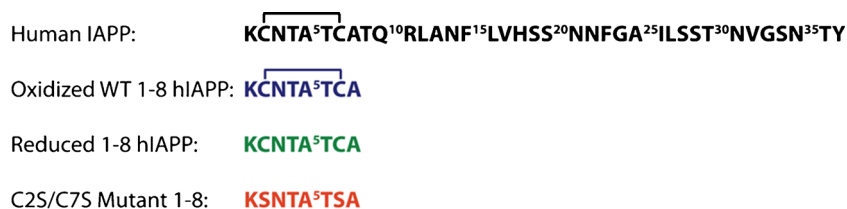


**Figure 1.** Sequences of the peptides studied in this work; the oxidized WT 1-8 residue fragment (WT<sub>1-8</sub><sup>ox</sup>) is indicated in blue, reduced 1-8 residue fragment (WT<sub>1-8</sub><sup>red</sup>) is indicated in green, and the cysteine to serine double mutant fragment (C2S/C7S<sub>1-8</sub>) is indicated in orange. The presence of a disulfide bond is indicated by a bracket. All of the peptides contain an amidated C-terminus. The sequence of full length hIAPP is shown in black for comparison

by an electron multiplier detector. Total time for analysis is between 400 and 2000 $\mu$ s.

Ion drift is affected by two factors; a uniform electric field,  $E$ , applied across the cell as well as collisions with the cell buffer gas. These two opposing forces result in a constant drift velocity proportional to the electric field with an ion mobility proportionality constant  $K$ ;

$$v_d = K \cdot E \quad (1)$$

The ion mobility is dependent upon the buffer gas temperature  $T$  and pressure  $P$ ; ion mobility is typically expressed without this dependence as a reduced mobility,  $K_0$ . The electric field is generated by a fixed voltage  $V$  across a drift cell of length  $L$ ;

$$K_0 = K \frac{P}{760 \text{ Torr}} \frac{273 \text{ K}}{T} \quad E = \frac{V}{L} \quad (2)$$

The reduced mobility can therefore be determined by plotting drift time as a function of pressure to voltage ( $P/V$ ) ratios;

$$v_d = \frac{L}{t_d} = K \cdot E \quad t_d = \frac{L}{K \cdot E} = \frac{L^2 (273 \text{ K})}{K_0 (760 \text{ Torr}) T} \cdot \frac{P}{V} \quad (3)$$

Ion mobility is then directly related to the ion's collision cross section via the collision theory of gases [53];

$$K_0 = \left( \frac{3e}{16N_0} \right) \left( \frac{2\pi}{\mu k_B T} \right)^{\frac{1}{2}} \frac{1}{\sigma} \quad (4)$$

where  $e$  is the ionic charge,  $N_0$  is the buffer gas number density,  $\mu$  is the reduced mass of the ion and buffer gas, and  $\sigma$  is the collision cross section.

### Molecular Dynamics

Explicit solvent temperature-REMD (T-REMD) simulations were performed for the wildtype 1-8 residue fragment (WT<sub>1-8</sub><sup>ox</sup>, containing a disulfide bond between the second and seventh cysteine residues), the reduced 1-8 residue fragment (WT<sub>1-8</sub><sup>red</sup>), and the cysteine  $\rightarrow$  serine C2S/C7S mutant fragment (C2S/C7S<sub>1-8</sub>) using the GROMACS 4.5.3 package and the all-atom Optimized Potentials for Liquid Simulations (OPLS-AA) force field in TIP3P water [54–56]. The peptide monomers have charged termini throughout the simulation, assuming neutral pH. The initial structure was minimized using the steepest decent method and solvated in a TIP3P water box. The size of the solvated cubic system was 4.50nm for peptide fragment dimer and tetramer simulations. In each system, negative charge chlorine ions were added to neutralize the system. Solvent and volume equilibration simulations in NPT ensemble ( $T=300\text{K}$  and  $P=1\text{bar}$ ) were performed to optimize the box size, followed by 6-ns NVT equilibration at 300K. The LINCS algorithm was employed to constrain bonds

between heavy atoms and hydrogen [57], and the SETTLE algorithm was used for water molecules [58]. These constraints allowed an integration time step of 2.0fs. The electrostatic and dispersion forces were computed with a real space cutoff of 1.2nm, and particle mesh Ewald method was used to treat long-range electrostatics [59]. The temperature was maintained by the Nose-Hoover thermostat [60]. The temperature and pressure coupling constants were 0.1 and 1.0ps, respectively. The equations of motion were integrated according to the leap-frog algorithm.

The initial guess for temperatures in T-REMD simulations (24 replicas for dimer and 32 replicas for tetramers) was taken from Patriksson and Spoel's temperature predictor (<http://folding.bmc.uu.se/remd/index.php>) and then adjusted to obtain the exchange rate of approximately 20%–25% [61]. Temperature lists can be found in the [supporting information](#).

Each replica was equilibrated at the desired temperature for 12ns before the production run for T-REMD began. Exchanges between replicas were attempted every 2ps. The production run was 300-ns long per replica for dimers and 400-ns per replica for tetramers. Only the last 150-ns data of the trajectory at 299K were subjected to analysis (Supplementary Figure S5). Clustering was performed using the Daura algorithm [62]. In order to obtain theoretical cross sections, 50 structures per cluster were subjected to a short minimization in the gas phase to mimic the desolvation process after the electrospray ionization process. After that, the theoretical cross sections were computed using the projected superposition approximation (PSA) method available at (<http://luschka.bic.ucsb.edu:8080/WebPSA/index.jsp>) and the average values were reported [63, 64].

### Atomic Force Microscopy

AFM experiments were carried out in tapping mode in air using an MFP-3D Atomic Force Microscope (Asylum Research, Goleta, CA, USA). A silicon probe was used with a cantilever spring constant of 7N/m and a resonant frequency of 155kHz (MikroMasch USA, Lady's Island, SC, USA). Protein incubation conditions matched those used in the IMS-MS experiments. Oxidized and mutant peptide fragment samples were incubated in 1:1 methanol:water; chemically reduced peptide samples were incubated with TCEP reducing agent at a 10:1 ratio of reducing agent to peptide. Five  $\mu$ L aliquots were removed at defined times over the course of incubation and deposited on freshly cleaved V1-grade mica (TedPella, Redding, CA, USA). The samples were then dried in a vacuum desiccator. Height analysis of globular aggregates was performed using a mask at 1nm to the image and adjusting to include all aggregates in the image. A particle analysis routine within the MFP-3D software was then applied.

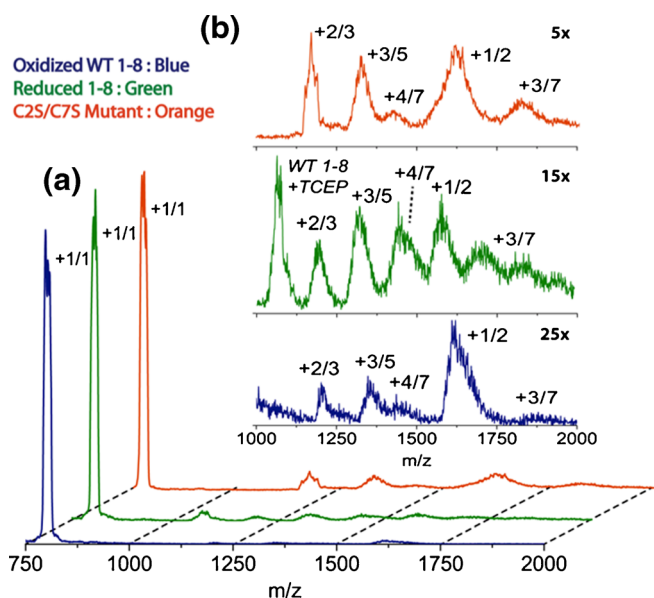


**Figure 2.** Mass spectra of IAPP peptide fragments at 50  $\mu\text{M}$  and 7.4 pH.  $\text{WT}_{1-8}^{\text{ox}}$  is indicated in blue,  $\text{WT}_{1-8}^{\text{red}}$  is indicated in green, and  $\text{C2S/C7S}_{1-8}$  is indicated in orange. Spectra are annotated by  $z/n$  where  $z$  is the charge and  $n$  the oligomer number.  $\text{WT}_{1-8}^{\text{red}}$  shows an additional peak not present in the other spectra corresponding to an adduction of the peptide and the TCEP reducing agent

## Results and Discussion

### *Early Oligomer Formation Probed by IMS-MS Reveals a Distinct Pathway for the Aggregation of $\text{WT}_{1-8}^{\text{ox}}$ Compared to Those of $\text{WT}_{1-8}^{\text{red}}$ and $\text{C2S/C7S}_{1-8}$*

Positive-ion mass-spectra showed similar predominant features for all three peptide fragments with peaks corresponding to a range of oligomers up to heptamer (Figure 2b).  $\text{WT}_{1-8}^{\text{red}}$  has an additional peak at 1070  $m/z$  not found in the other samples; this is likely a complex between a singly charged peptide and an adduct of the reducing agent, *tris*(2-carboxyethyl)phosphine (TCEP) (810amu + 250amu). All three samples show extensive oligomerization at both vesicular (pH=5.5) and physiological pH (pH=7.4). Arrival time distributions (ATDs) of all major features were collected and representative ATDs are shown in Figure 3. Several aspects of the ATDs are of note. In the  $z/n = +1/1$  ATD more doubly charged dimers are seen for the reduced  $\text{WT}_{1-8}^{\text{red}}$  versus the oxidized  $\text{WT}_{1-8}^{\text{ox}}$  or mutant  $\text{C2S/C7S}_{1-8}$  (Figure 3a). Secondly, more higher-order oligomers are seen in the reduced and mutant  $z/n = +1/2$  ATDs than in  $\text{WT}_{1-8}^{\text{ox}}$  (Figure 3b). This suggests that the presence of the disulfide bond inhibits oligomer formation. For all fragments the +2/2 oligomers show larger cross sections than the corresponding singly charged dimers. This is likely the result of charge

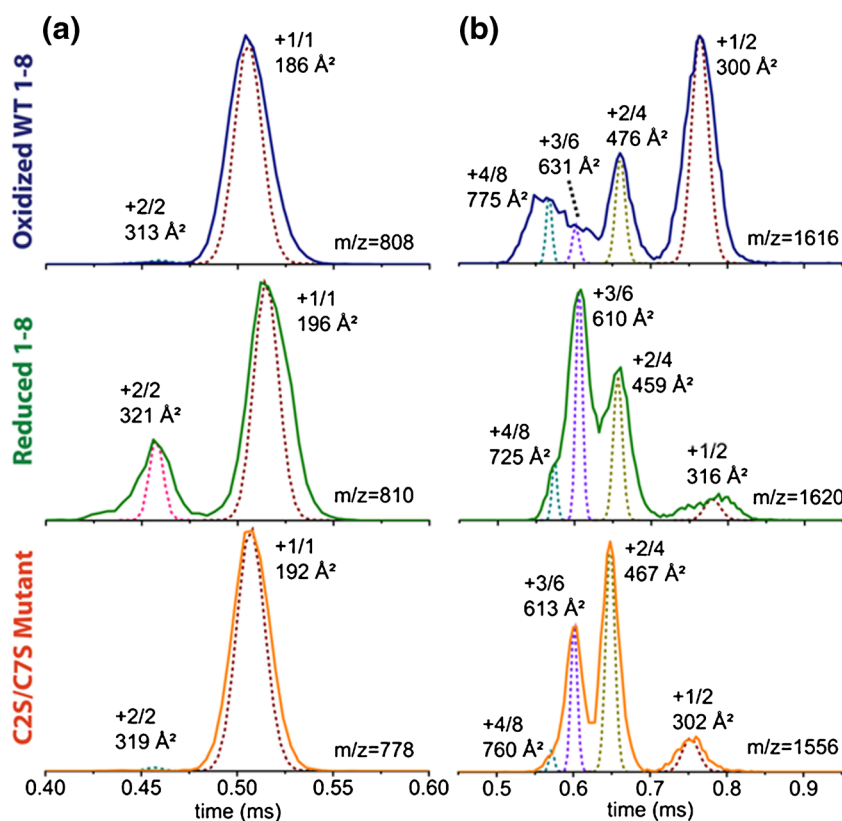


**Figure 3.** Representative ATD of the human IAPP fragment peptides at 50  $\mu\text{M}$  and 7.4 pH;  $\text{WT}_{1-8}^{\text{ox}}$  is indicated in blue,  $\text{WT}_{1-8}^{\text{red}}$  is indicated in green, and  $\text{C2S/C7S}_{1-8}$  is indicated in orange. All peaks are annotated by  $z/n$ , where  $z$  is the charge and  $n$  the oligomer number. The cross sections for all peaks are also noted. The injection energy is 40 V. Each peak is fit using the procedure described in the supporting information

**Table 1.** Collision Cross Section in  $\text{\AA}^2$  of IAPP Fragments in the  $z/n = +1/1$  and  $+1/2$  ATDs\*

Charge State Peptide	+1 Monomer	+2 Dimer	+1 Dimer	+2 Tetramer	+3 Hexamer	+4 Octamer
Oxidized WT 1-8	186	313	300	476	631	775
Reduced 1-8	196	321	316	459	610	725
C2S/C7S mutant 1-8	192	319	302	467	613	760

\*Percent deviation for all measurements less than  $\pm 2\%$ .

repulsion between lysines at position 1, indicating that these amino acids are in close proximity within the dimer. Comparing relative collision cross sections, the higher-order oligomers of the  $WT_{1-8}^{\text{red}}$  and  $C2S/C7S_{1-8}$  peptides are more compact than those of the  $WT_{1-8}^{\text{ox}}$  peptide (Table 1), whereas the lower-order  $WT_{1-8}^{\text{ox}}$  oligomers are smaller than those of the reduced or mutant peptides. The REMD simulations of the dimers confirm this trend, with  $WT_{1-8}^{\text{red}}$  and  $C2S/C7S_{1-8}$  favoring extended conformations with extensive intermolecular bonding, whereas  $WT_{1-8}^{\text{ox}}$  takes on compact conformations with low intermolecular bonding (Figure 4). The REMD results also

show  $WT_{1-8}^{\text{ox}}$  has fewer hydrogen bonds between monomers than  $WT_{1-8}^{\text{red}}$  and  $C2S/C7S_{1-8}$  in the tetramers (Figure 5e, f). Taken together, the IMS-MS and REMD results suggest  $WT_{1-8}^{\text{ox}}$  aggregates via a different pathway than the peptides without a disulfide bond.

### AFM Reveals $WT_{1-8}^{\text{red}}$ and $C2S/C7S_{1-8}$ Show Opposite Morphological Transformations

AFM results allow the extrapolation of aggregation trends and morphologies for larger oligomers in solution (Figure 6).  $WT_{1-}$

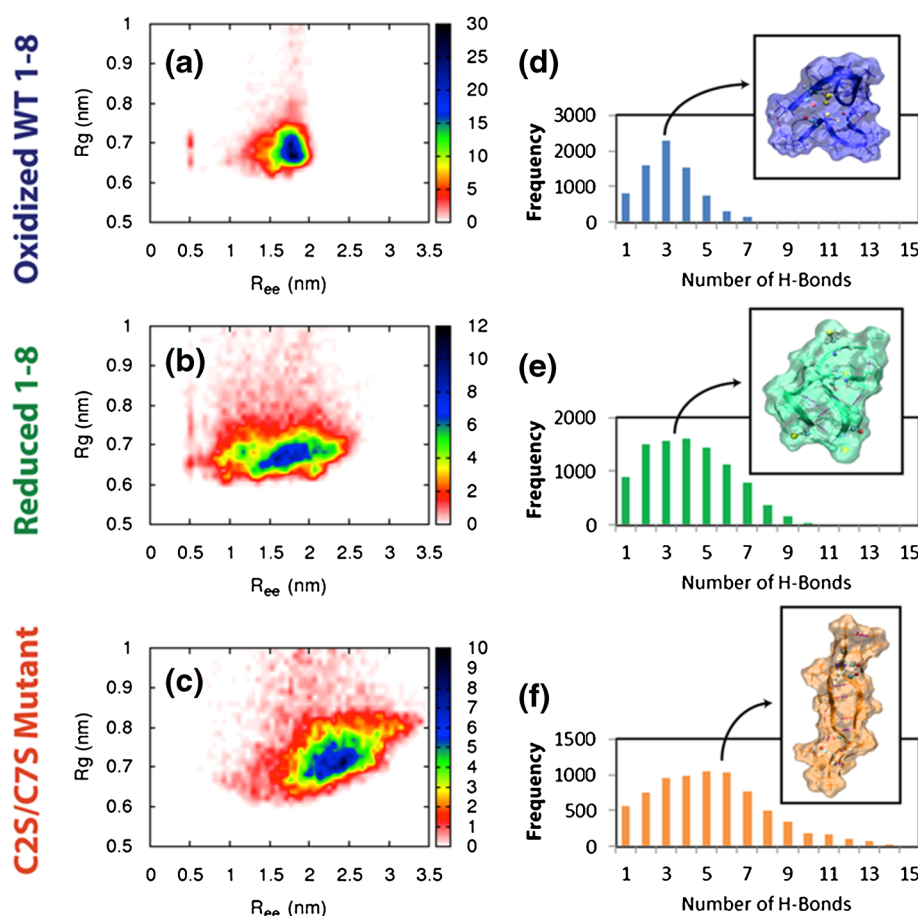


**Figure 4.** Conformational spaces sampled by the peptide dimers and distributions of the number of hydrogen bonds between peptide monomers for  $WT_{1-8}^{\text{ox}}$  (a), (d),  $WT_{1-8}^{\text{red}}$  (b), (e), and  $C2S/C7S_{1-8}$  (c), (f). A sample structure containing the mean number of hydrogen bonds is shown by each distribution. The potential mean force (PMF) is generated from the distributions of the end-to-end distances ( $R_{ee}$ , nm) of the dimer;  $R_{ee} = (R_{ee1}^2 + R_{ee2}^2)^{1/2}$ , and the distributions of the radius of gyration ( $R_g$ , nm). The disulfide bonds keep the  $WT_{1-8}^{\text{ox}}$  dimers in a narrow conformational space, whereas both  $C2S/C7S_{1-8}$  and  $WT_{1-8}^{\text{red}}$  dimers adopt a wider range of structures including significant populations of extended structures ( $R_{ee} \geq 2$  nm). The extended structures are stabilized through inter-chain hydrogen bonding, with an average of five hydrogen bonds per structure

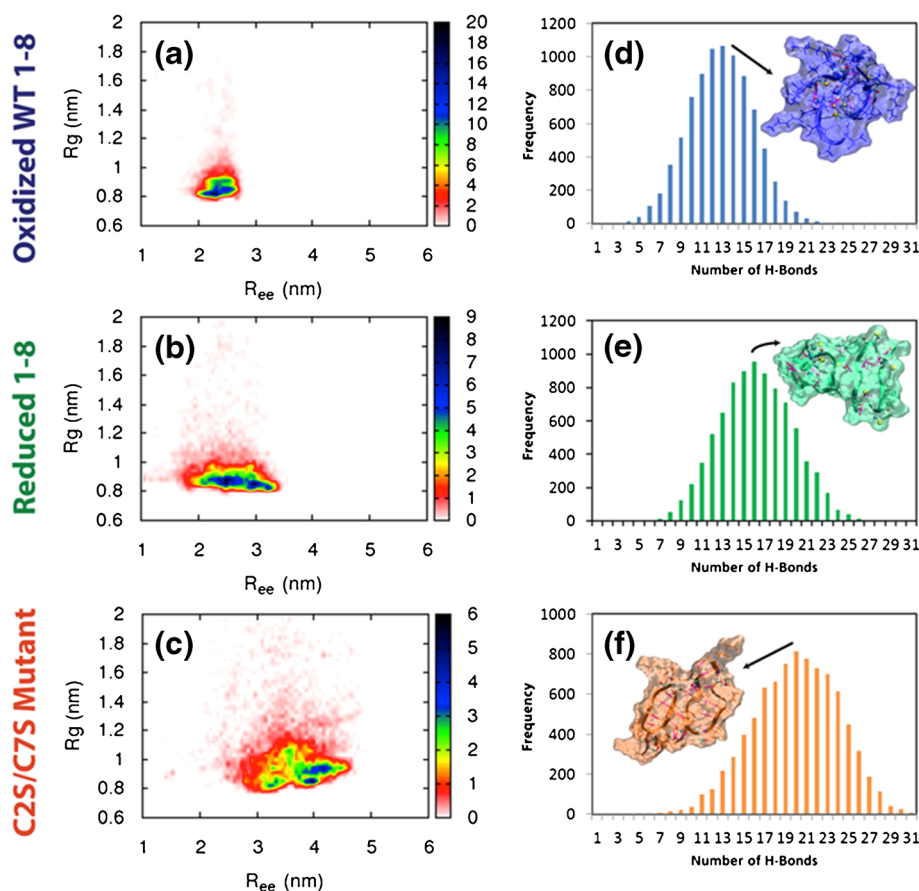


**Figure 5.** Conformational spaces sampled by the peptide tetramers and distributions of the number of hydrogen bonds between peptide monomers for  $WT_{1-8}^{ox}$  (a), (d),  $WT_{1-8}^{red}$  (b), (e), and C2S/C7S $_{1-8}$  (c), (f). A sample structure containing the mean number of hydrogen bonds is shown by each distribution. The potential mean force (PMF) is generated from the distributions of the end-to-end distances ( $R_{ee}$ , nm) of the tetramer;  $R_{ee} = (R_{ee1}^2 + R_{ee2}^2 + R_{ee3}^2 + R_{ee4}^2)^{1/2}$ , and the distributions of the radius of gyration ( $R_g$ , nm). The  $WT_{1-8}^{ox}$  tetramers sample only compact structures with small amounts of hydrogen bond formation, similar to its dimers. The C2S/C7S $_{1-8}$  prefers to adopt elongated structure (the majority have  $R_{ee} > 3$  nm), however, its conformational space is disordered with multiple distinct local minima. The conformational space of  $WT_{1-8}^{red}$  is less disordered than that of the mutant with significant hydrogen bond formation

$_{8}^{ox}$  exhibited relatively slow, gradual fibril growth over the course of the 1-hour incubation period consistent with oligomer trends observed by IMS-MS (Figure 6a). After 5min of incubation, few fibrils were seen on the mica substrate with the dominant structure being small, unstructured globular aggregates with an average height of  $1.00 \pm (0.25)$  nm. Fibril-like structures that are present are approximately 0.5nm in height. After 30min, there were indications of growth via a seeding core mechanism; fibrils with heights of 0.5nm were observed growing from central cores of  $\sim 1$ nm in height. This growth motif has been previously observed for the full-length hIAPP peptide [65, 66]. From this time onward, growth of several fibrils from a central seed becomes a pervasive growth motif. After 60min, a large degree of lateral growth has occurred and the fibril diameters are much larger, ranging from one to several tens of nanometers. The three representative images shown in Figure 6a reveal that fibril nucleating cores progressively increase in size with time. These data, along with the apparent bundling of fibrils when incubation time is extended to 24h

(Supplementary Figure S2), are consistent with observations of  $WT_{1-8}^{ox}$  made by Cope et al. but the fibrils we observe show more curvature [43]. Given the relatively low amount of intermolecular hydrogen bonding predicted by the REMD simulations for smaller oligomers, the observed fibril bundling could be a result of lateral stabilization that allows for the increase in linear growth and the observed curvature.

As seen in Figure 6b, c, both  $WT_{1-8}^{red}$  and C2S/C7S $_{1-8}$  rapidly form highly ordered aggregate structures (Figure 6, 5min), consistent with both the higher order oligomerization seen in the IMS-MS experiments and the extensive intermolecular hydrogen bonding predicted by REMD. C2S/C7S $_{1-8}$  fibrils of sizes ranging in width from 1nm at the smallest to 10nm at the largest were observed after just 5min of incubation (Figure 6c). At longer incubation times, these fibrils appear to self-associate resulting in an interwoven morphology (Figure 6c, 30min) that then rearranges into short, needle-like aggregates (Figure 6c, 60min).  $WT_{1-8}^{red}$  also formed ordered aggregates rapidly; however, its time evolution differs from

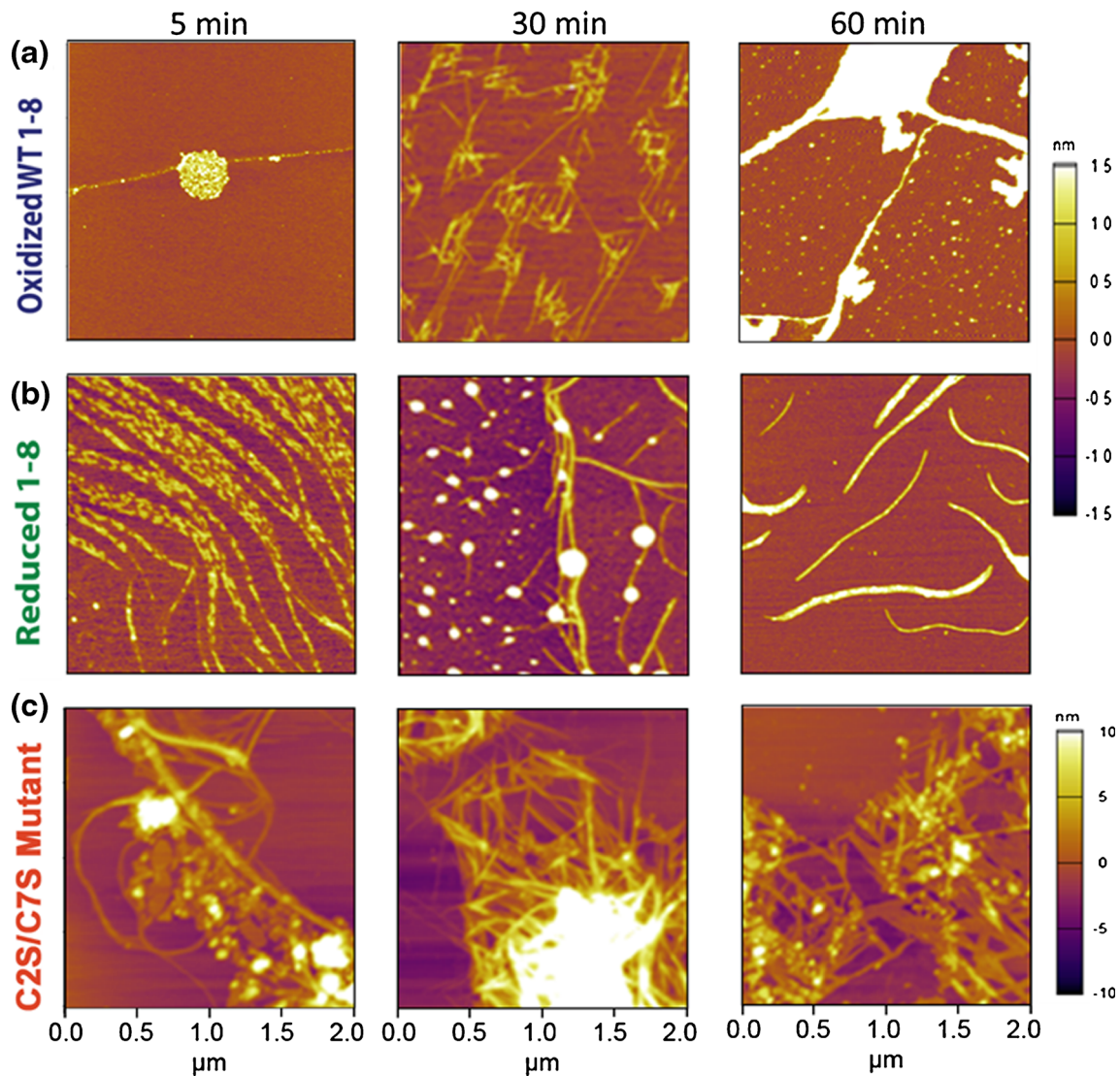


**Figure 6.** Time-lapse incubation of WT<sub>1-8</sub><sup>ox</sup> **(a)**, WT<sub>1-8</sub><sup>red</sup> **(b)**, and C2S/C7S<sub>1-8</sub> **(c)** fragments at 50  $\mu$ M and 7.4 pH with incubation times of 5, 30, and 60 min. WT 1-8 hIAPP shows gradual fibril growth over the course of incubation. WT<sub>1-8</sub><sup>red</sup> shows growth from initially short, closely associated structures into more traditional fibril-like aggregates. C2S/C7S<sub>1-8</sub> shows rapid ordering into fibril-like aggregates after only 5 min followed by self-aggregation of these fibrils and further conversion into needle-like structures

C2S/C7S<sub>1-8</sub>. Short, closely associated fibril structures are favored at short incubation times and more extended fibrils favored at longer incubation times (Figure 6b). After 1h, both WT<sub>1-8</sub><sup>red</sup> and C2S/C7S<sub>1-8</sub> exhibited feature lengths significantly shorter than WT<sub>1-8</sub><sup>ox</sup>. This could explain the apparent lack of aggregation observed in prior studies for WT<sub>1-8</sub><sup>red</sup>, given that structures of this size would not be visible under a standard light microscope [43]. Again it is intriguing that the peptides for which REMD predicted higher intermolecular bonding appear to follow a discrete aggregation pathway disparate from WT<sub>1-8</sub><sup>ox</sup>, a result consistent with IMS-MS data.

## Conclusions

The presence of the disulfide bond in the N-terminal fragment does not completely inhibit self-aggregation of the fragment,

but reduction of the disulfide bond or its removal by mutation increases the rate of aggregation. Overall, IMS-MS, REMD simulations, and AFM indicate WT<sub>1-8</sub><sup>ox</sup> is capable of forming stable aggregates along an entirely different pathway than both WT<sub>1-8</sub><sup>red</sup> and C2S/C7S<sub>1-8</sub>. WT<sub>1-8</sub><sup>red</sup> and C2S/C7S<sub>1-8</sub> form extended oligomer conformations with high intermolecular hydrogen bonding (Figures 4 and 5). AFM images recorded at short incubation times corroborate these conclusions, with WT<sub>1-8</sub><sup>red</sup> and C2S/C7S<sub>1-8</sub> showing extensive aggregation and rearrangement. Long-term macroscopic fibril formation varies drastically between the peptides, WT<sub>1-8</sub><sup>ox</sup> prefers extended fibril bundling seeded by globular aggregates; WT<sub>1-8</sub><sup>red</sup> forms short fibrils of varying widths, and C2S/C7S<sub>1-8</sub> favors densely packed needle-like structures. These observations, coupled with the REMD results, suggest that the cleavage of the disulfide bond has an agonistic effect toward oligomerization of the

full hIAPP peptide by increasing the probability of intermolecular hydrogen bonding and  $\beta$ -sheet formation. Perhaps the most important conclusion we make is that the 2-7 disulfide bond at the N-terminus limits the aggregation of the peptide relative to both the reduced and mutated peptides. This occurs primarily due to a significant reduction in intermolecular hydrogen bonds relative to the noncyclic peptides and suggests the disulfide bond may actually protect full-length hIAPP from amyloid formation. This central conclusion is at odds with the conclusion of Cope et al. [43], who concluded that “loop-loop” interaction might enhance hIAPP oligomerization and could be a target for therapeutic intervention.

## Acknowledgments

The authors thank William Wonderly for his assistance with sample preparation. Support from the National Science Foundation under grant CHE-1301032 (M.T.B.) and the National Institutes of Health GM078114 (D.P.R.) is gratefully acknowledged. A.G.W. was supported in part by a GAANN fellowship from the Department of Education.

## References

1. Westermark, P., Andersson, A., Westermark, G.T.: Islet amyloid polypeptide, islet amyloid, and diabetes mellitus. *Physiol. Rev.* **91**, 795–826 (2011)
2. Lin, C.Y., Gurlo, T., Kaye, R., Butler, A.E., Haataja, L., Glabe, C.G., Butler, P.C.: Toxic human islet amyloid polypeptide (h-IAPP) oligomers are intracellular, and vaccination to induce anti-toxic oligomer antibodies does not prevent h-IAPP-induced beta-cell apoptosis in h-IAPP transgenic mice. *Diabetes* **56**, 1324–1332 (2007)
3. Haataja, L., Gurlo, T., Huang, C.J., Butler, P.C.: Islet amyloid in type 2 diabetes, and the toxic oligomer hypothesis. *Endocr. Rev.* **29**, 303–316 (2008)
4. Laybutt, D.R., Preston, A.M., Akerfeldt, M.C., Kench, J.G., Busch, A.K., Biankin, A.V., Biden, T.J.: Endoplasmic reticulum stress contributes to beta cell apoptosis in type 2 diabetes. *Diabetologia* **50**, 752–763 (2007)
5. Hull, R.L., Westermark, G.T., Westermark, P., Kahn, S.E.: Islet amyloid: a critical entity in the pathogenesis of type 2 diabetes. *J. Clin. Endocrinol. Metab.* **89**, 3629–3643 (2004)
6. Westermark, P., Wernstedt, C., Wilander, E., Hayden, D.W., Obrien, T.D., Johnson, K.H.: Amyloid fibrils in human insulinoma and islets of langerhans of the diabetic cat are derived from a neuropeptide-like protein also present in normal islet cells. *Proc. Natl. Acad. Sci. U. S. A.* **84**, 3881–3885 (1987)
7. Cooper, G.J.S., Willis, A.C., Clark, A., Turner, R.C., Sim, R.B., Reid, K.B.M.: Purification and characterization of a peptide from amyloid-rich pancreases of type-2 diabetic-patients. *Proc. Natl. Acad. Sci. U. S. A.* **84**, 8628–8632 (1987)
8. Cao, P., Abedini, A., Raleigh, D.P.: Aggregation of islet amyloid polypeptide: from physical chemistry to cell biology. *Curr Opin Struct Biol* **23**, 82–89 (2013)
9. Gedulin, B., Cooper, G.J.S., Young, A.A.: Amylin secretion from the perfused pancreas - dissociation from insulin and abnormal elevation in insulin-resistant diabetic rats. *Biochem Biophys Res Commun* **180**, 782–789 (1991)
10. Kaye, R., Bernhagen, J., Greenfield, N., Sweimeh, K., Brunner, H., Voelter, W., Kapurmiotu, A.: Conformational transitions of islet amyloid polypeptide (IAPP) in amyloid formation in vitro. *J. Mol. Biol.* **287**, 781–796 (1999)
11. Lutz, T.A.: The role of amylin in the control of energy homeostasis. *Am J Physiol Regul Integr Comp Physiol* **298**, R1475–R1484 (2010)
12. Westermark, G.T., Westermark, P., Berne, C., Korsgren, O., Transplanta, N.N.C.I.: Widespread amyloid deposition in transplanted human pancreatic islets. *N Engl J Med* **359**, 977–979 (2008)
13. Potter, K.J., Abedini, A., Marek, P., Klimek, A.M., Butterworth, S., Driscoll, M., Baker, R., Nilsson, M.R., Warnock, G.L., Oberholzer, J., Bertera, S., Trucco, M., Korbitt, G.S., Fraser, P.E., Raleigh, D.P., Verchere, C.B.: Islet amyloid deposition limits the viability of human islet grafts but not porcine islet grafts. *Proc. Natl. Acad. Sci. U. S. A.* **107**, 4305–4310 (2010)
14. Stefani, M.: Protein misfolding and aggregation: new examples in medicine and biology of the dark side of the protein world. *BBA-Mol Basis Dis* **1739**, 5–25 (2004)
15. Porat, Y., Kolusheva, S., Jelinek, R., Gazit, E.: The human islet amyloid polypeptide forms transient membrane-active prefibrillar assemblies. *Biochemistry* **42**, 10971–10977 (2003)
16. Kaye, R., Head, E., Thompson, J.L., McIntire, T.M., Milton, S.C., Cotman, C.W., Glabe, C.G.: Common structure of soluble amyloid oligomers implies common mechanism of pathogenesis. *Science* **300**, 486–489 (2003)
17. Bleiholder, C., Dupuis, N.F., Wytttenbach, T., Bowers, M.T.: Ion mobility-mass spectrometry reveals a conformational conversion from random assembly to beta-sheet in amyloid fibril formation. *Nat. Chem.* **3**, 172–177 (2011)
18. Sitkiewicz, E., Kloniecki, M., Poznanski, J., Bal, W., Dadlez, M.: Factors influencing compact-extended structure equilibrium in oligomers of a beta 1-40 peptide-an ion mobility mass spectrometry study. *J. Mol. Biol.* **426**, 2871–2885 (2014)
19. Woods, L.A., Platt, G.W., Hellewell, A.L., Hewitt, E.W., Homans, S.W., Ashcroft, A.E., Radford, S.E.: Ligand binding to distinct states diverts aggregation of an amyloid-forming protein. *Nat. Chem. Biol.* **7**, 730–739 (2011)
20. Young, L.M., Cao, P., Raleigh, D.P., Ashcroft, A.E., Radford, S.E.: Ion mobility spectrometry-mass spectrometry defines the oligomeric intermediates in amylin amyloid formation and the mode of action of inhibitors. *J. Am. Chem. Soc.* **136**, 660–670 (2014)
21. Young, L.M., Saunders, J.C., Mahood, R.A., Revill, C.H., Foster, R.J., Tu, L.H., Raleigh, D.P., Radford, S.E., Ashcroft, A.E.: Screening and classifying small-molecule inhibitors of amyloid formation using ion mobility spectrometry-mass spectrometry. *Nat. Chem.* **7**, 73–81 (2015)
22. Dupuis, N.F., Wu, C., Shea, J.E., Bowers, M.T.: Human islet amyloid polypeptide monomers form ordered beta-hairpins: a possible direct amyloidogenic precursor. *J. Am. Chem. Soc.* **131**, 18283–18292 (2009)
23. Dupuis, N.F., Wu, C., Shea, J.E., Bowers, M.T.: The amyloid formation mechanism in human IAPP: dimers have beta-strand monomer-monomer interfaces. *J. Am. Chem. Soc.* **133**, 7240–7243 (2011)
24. Susa, A.C., Wu, C., Bernstein, S.L., Dupuis, N.F., Wang, H., Raleigh, D.P., Shea, J.E., Bowers, M.T.: Defining the molecular basis of amyloid inhibitors: human islet amyloid polypeptide-insulin interactions. *J. Am. Chem. Soc.* **136**, 12912–12919 (2014)
25. Nilsson, M.R., Raleigh, D.P.: Analysis of amylin cleavage products provides new insights into the amyloidogenic region of human amylin. *J. Mol. Biol.* **294**, 1375–1385 (1999)
26. Tracz, S.M., Abedini, A., Driscoll, M., Raleigh, D.P.: Role of aromatic interactions in amyloid formation by peptides derived from human amylin. *Biochemistry* **43**, 15901–15908 (2004)
27. Gilead, S., and Gazit, E.: The role of the 14-20 domain of the islet amyloid polypeptide in amyloid formation. *Exp Diabetes Res* **2008**, 256954 (2008)
28. Scrocchi, L.A., Chen, Y., Waschuk, S., Wang, F., Cheung, S., Darabie, A.A., McLaurin, J., Fraser, P.E.: Design of peptide-based inhibitors of human islet amyloid polypeptide fibrillogenesis. *J. Mol. Biol.* **318**, 697–706 (2002)
29. Kapurmiotu, A., Schmauder, A., Tenidis, K.: Structure-based design and study of non-amyloidogenic, double N-methylated IAPP amyloid core sequences as inhibitors of IAPP amyloid formation and cytotoxicity. *J. Mol. Biol.* **315**, 339–350 (2002)
30. Sellin, D., Yan, L.M., Kapurmiotu, A., Winter, R.: Suppression of IAPP fibrillation at anionic lipid membranes via IAPP-derived amyloid inhibitors and insulin. *Biophys. Chem.* **150**, 73–79 (2010)
31. Buchanan, L.E., Dunkelberger, E.B., Tran, H.Q., Cheng, P.N., Chiu, C.C., Cao, P., Raleigh, D.P., de Pablo, J.J., Nowick, J.S., Zanni, M.T.: Mechanism of IAPP amyloid fibril formation involves an intermediate with a transient beta-sheet. *Proc. Natl. Acad. Sci. U. S. A.* **110**, 19285–19290 (2013)
32. Westermark, P., Engstrom, U., Johnson, K.H., Westermark, G.T., Betsholtz, C.: Islet amyloid polypeptide - pinpointing amino-acid-residues linked to amyloid fibril formation. *Proc. Natl. Acad. Sci. U. S. A.* **87**, 5036–5040 (1990)



33. Tenidis, K., Waldner, M., Bernhagen, J., Fischle, W., Bergmann, M., Weber, M., Merkle, M.L., Voelter, W., Brunner, H., Kapurniotu, A.: Identification of a penta- and hexapeptide of islet amyloid polypeptide (IAPP) with amyloidogenic and cytotoxic properties. *J. Mol. Biol.* **295**, 1055–1071 (2000)
34. Scrocchi, L.A., Ha, K., Chen, Y., Wu, L., Wang, F., Fraser, P.E.: Identification of minimal peptide sequences in the (8-20) domain of human islet amyloid polypeptide involved in fibrillogenesis. *J. Struct. Biol.* **141**, 218–227 (2003)
35. Gazit, E.: Mechanistic studies of the process of amyloid fibrils formation by the use of peptide fragments, and analogues: implications for the design of fibrillization inhibitors. *Curr. Med. Chem.* **9**, 1725–1735 (2002)
36. Roberts, A.N., Leighton, B., Todd, J.A., Cockburn, D., Schofield, P.N., Sutton, R., Holt, S., Boyd, Y., Day, A.J., Foot, E.A., Willis, A.C., Reid, K.B.M., Cooper, G.J.S.: Molecular and functional-characterization of amylin, a peptide associated with type-2 diabetes-mellitus. *Proc. Natl. Acad. Sci. U. S. A.* **86**, 9662–9666 (1989)
37. Cornish, J., Callon, K.E., Lin, C.Q.X., Xiao, C.L., Mulvey, T.B., Coy, D.H., Cooper, G.J.S., Reid, I.R.: Dissociation of the effects of amylin on osteoblast proliferation and bone resorption. *Am J Physiol-Endocrinol Metab* **274**, E827–E833 (1998)
38. Hay, D.L., Christopoulos, G., Christopoulos, A., Poyner, D.R., Sexton, P.M.: Pharmacological discrimination of calcitonin receptor: receptor activity-modifying protein complexes. *Mol. Pharmacol.* **67**, 1655–1665 (2005)
39. Wang, Z.L., Bennet, W.M., Ghatei, M.A., Byfield, P.G.H., Smith, D.M., Bloom, S.R.: Influence of islet amyloid polypeptide and the 8-37 fragment of islet amyloid polypeptide on insulin release from perfused rat islets. *Diabetes* **42**, 330–335 (1993)
40. Goldsbury, C., Goldie, K., Pellaud, J., Seelig, J., Frey, P., Muller, S.A., Kistler, J., Cooper, G.J.S., Aebi, U.: Amyloid fibril formation from full-length and fragments of amylin. *J. Struct. Biol.* **130**, 352–362 (2000)
41. Koo, B.W., Miranker, A.D.: Contribution of the intrinsic disulfide to the assembly mechanism of islet amyloid. *Protein Sci.* **14**, 231–239 (2005)
42. Jayasinghe, S.A., Langen, R.: Identifying structural features of fibrillar islet amyloid polypeptide using site-directed spin labeling. *J. Biol. Chem.* **279**, 48420–48425 (2004)
43. Cope, S.M., Shinde, S., Best, R.B., Ghirlanda, G., Vaiana, S.M.: Cyclic N-terminal loop of amylin forms non amyloid fibers. *Biophys. J.* **105**, 1661–1669 (2013)
44. Lanucara, F., Holman, S.W., Gray, C.J., Eyers, C.E.: The power of ion mobility-mass spectrometry for structural characterization and the study of conformational dynamics. *Nat. Chem.* **6**, 281–294 (2014)
45. Jureczko, E., Barran, P.E.: How useful is ion mobility mass spectrometry for structural biology? The relationship between protein crystal structures and their collision cross sections in the gas phase. *Analyst* **136**, 20–28 (2011)
46. Adamcik, J., Mezzenga, R.: Study of amyloid fibrils via atomic force microscopy. *Curr Opin Colloid Interface* **17**, 369–376 (2012)
47. Smith, J.F., Knowles, T.P.J., Dobson, C.M., MacPhee, C.E., Welland, M.E.: Characterization of the nanoscale properties of individual amyloid fibrils. *Proc. Natl. Acad. Sci. U. S. A.* **103**, 15806–15811 (2006)
48. Adamcik, J., Jung, J.M., Flakowski, J., De Los Rios, P., Dietler, G., Mezzenga, R.: Understanding amyloid aggregation by statistical analysis of atomic force microscopy images. *Nat. Nanotechnol.* **5**, 423–428 (2010)
49. Ahmed, M., Davis, J., Aucoin, D., Sato, T., Ahuja, S., Aimoto, S., Elliott, J.I., Van Nostrand, W.E., Smith, S.O.: Structural conversion of neurotoxic amyloid-beta(1-42) oligomers to fibrils. *Nat. Struct. Mol. Biol.* **17**, 561–U556 (2010)
50. Marek, P., Woys, A.M., Sutton, K., Zanni, M.T., Raleigh, D.P.: Efficient microwave-assisted synthesis of human islet amyloid polypeptide designed to facilitate the specific incorporation of labeled amino acids. *Org. Lett.* **12**, 4848–4851 (2010)
51. Abedini, A., Raleigh, D.P.: Incorporation of pseudoproline derivatives allows the facile synthesis of human IAPP, a highly amyloidogenic and aggregation-prone polypeptide. *Org. Lett.* **7**, 693–696 (2005)
52. Wyttenbach, T., Kemper, P.R., Bowers, M.T.: Design of a new electrospray ion mobility mass spectrometer. *Int J Mass Spectrom* **212**, 13–23 (2001)
53. Mason, E.A., McDaniel, E.W.: Transport properties of ions in gases. Wiley, New York (1988)
54. Jorgensen, W.L., Tiradorives, J.: The Opls potential functions for proteins - energy minimizations for crystals of cyclic-peptides and crambin. *J. Am. Chem. Soc.* **110**, 1657–1666 (1988)
55. Hess, B., Kutzner, C., van der Spoel, D., Lindahl, E.: GROMACS 4: algorithms for highly efficient, load-balanced, and scalable molecular simulation. *J Chem Theory Comput* **4**, 435–447 (2008)
56. Van der Spoel, D., Lindahl, E., Hess, B., Groenhof, G., Mark, A.E., Berendsen, H.J.C.: GROMACS: fast, flexible, and free. *J. Comput. Chem.* **26**, 1701–1718 (2005)
57. Hess, B., Bekker, H., Berendsen, H.J.C., Fraaije, J.G.E.M.: LINCS: a linear constraint solver for molecular simulations. *J. Comput. Chem.* **18**, 1463–1472 (1997)
58. Miyamoto, S., Kollman, P.A.: SETTLE: an analytical version of the shake and rattle algorithm for rigid water models. *J Comput Chem* **13**(952–962) (2004)
59. Darden, T., York, D., Pedersen, L.: Particle Mesh Ewald - an N. Log(N) method for Ewald sums in large systems. *J. Chem. Phys.* **98**, 10089–10092 (1993)
60. Evans, D.J., Holian, B.L.: The nose-hoover thermostat. *J. Chem. Phys.* **83**, 4069–4074 (1985)
61. Patriksson, A., van der Spoel, D.: A temperature predictor for parallel tempering simulations. *Phys. Chem. Chem. Phys.* **10**, 2073–2077 (2008)
62. Daura, X., Gademann, K., Jaun, B., Seebach, D., van Gunsteren, W.F., Mark, A.E.: Peptide folding: when simulation meets experiment. *Angew Chem Int Edit* **38**, 236–240 (1999)
63. Bleiholder, C., Wyttenbach, T., Bowers, M.T.: A novel projection approximation algorithm for the fast and accurate computation of molecular collision cross sections (I). *Int J Mass Spectrom* **308**, 1–10 (2011)
64. Bleiholder, C., Contreras, S., Do, T.D., Bowers, M.T.: A novel projection approximation algorithm for the fast and accurate computation of molecular collision cross sections (II). Model parameterization and definition of empirical shape factors for proteins. *Int J Mass Spectrom* **345**, 89–96 (2013)
65. Green, J.D., Goldsbury, C., Kistler, J., Cooper, G.J.S., Aebi, U.: Human amylin oligomer growth and fibril elongation define two distinct phases in amyloid formation. *J. Biol. Chem.* **279**, 12206–12212 (2004)
66. Patil, S.M., Mehta, A., Jha, S., Alexandrescu, A.T.: Heterogeneous amylin fibril growth mechanisms imaged by total internal reflection fluorescence microscopy. *Biochemistry* **50**, 2808–2819 (2011)